

Direct computation of the sound radiated by a high-Reynolds number, subsonic round jet

C. Bogey* and C. Bailly†

Laboratoire de Mécanique des Fluides et d'Acoustique
Ecole Centrale de Lyon, UMR CNRS 5509
36, av. Guy de Collongue, 69134 Ecully, France
<http://www.lmfa.ec-lyon.fr/autres/CAA/caaweb.html>

Abstract

An isothermal circular jet with a Mach number of $M = 0.9$ and a Reynolds number of $Re_D = 4 \times 10^5$ is computed by a compressible Large Eddy Simulation (LES) using a highly selective filtering. The flow development is shown not to depend on the location of the mesh grid boundaries. The flow and the sound field obtained directly from the LES are in good agreement with the corresponding measurements of the literature. The acoustic radiation displays also spectra and azimuthal correlation functions which behave as expected for a high Reynolds number jet. This demonstrates that the Reynolds number defined by the inflow conditions is actually preserved by the simulation. Furthermore, the two components of jet noise usually associated to large scales and to fine-scale turbulence respectively are apparently found.

1 Introduction

Direct Noise Computation (DNC) consists in calculating the sound field directly by solving the unsteady compressible flow equations.¹ Since the flow and sound fields are provided simultaneously, DNC is intended to allow further investigations on noise generation mechanisms. This motivation is strong for flows, such as subsonic jets, where noise sources are still not clearly identified. Direct Numerical simulation (DNS), resolving the full Navier-Stokes equations, can be used,² but its applications are limited to flows with low Reynolds numbers displaying a small range of turbulent scales. This is not the case with Large Eddy Simulation (LES), where only all the scales larger than the mesh grid size are calculated, which can theoretically deal with flows at any Reynolds number. For this reason, LES appears as an appropriate tool to investigate realistic turbulent flows. In the last few years, this methodology has been experimented to study the noise radiated by supersonic³ and subsonic⁴⁻⁸ jets. The latter simulations demonstrated the feasibility of DNC using LES for subsonic jets. However, moderate Reynolds numbers were often involved. For example, the first jet simulated by the authors⁴ was for a Mach number of $M = u_j/c_a = 0.9$ and for a Reynolds number of $Re_D = u_j D/\nu = 6.4 \times 10^4$ (u_j is the jet nozzle exit, c_a the ambient sound speed, D the jet diameter, and ν the molecular viscosity). Dealing with higher Reynolds numbers appears now necessary to discuss the full physics of jet noise.

*CNRS Research Scientist, christophe.bogey@ec-lyon.fr

†Assistant Professor, christophe.bailly@ec-lyon.fr

With this aim in view, the LES of a high Reynolds number circular jet is carried out in the present study. The jet is isothermal with $T_j = T_a$ (T_a is the ambient temperature). The Mach number is $M = 0.9$ and the jet diameter is chosen to be $D = 2$ cm yielding a Reynolds number of $Re_D = 4 \times 10^5$. Two simulations using mesh grids of different sizes, one extending far away downstream and one including a part of the acoustic field, are performed. The first motivation is to show that the flow development is not dependent on the location of the grid boundaries. The second one is to obtain flow and sound field properties corresponding to those typically found for jets with similar Reynolds numbers. This would imply that the effective Reynolds number of the jet is preserved by the numerical resolution, which is not evident with LES at high Reynolds numbers. For this, the present simulations are performed using a Navier-Stokes solver (ALESIA^{4,9}) developed for DNC, using low dispersive and low dissipative numerical schemes,¹⁰ and using efficient non-reflecting boundary conditions.¹¹ The feature of the solver is to take into account the effects of the lacking turbulent-energy dissipating scales, non resolved by the grid, through a high-order filtering instead of an eddy-viscosity model as usually. The filtering is built up to eliminate short waves but, unlike an eddy viscosity, does not affect the resolved scales. To demonstrate that the present simulations are then Reynolds-Number-Preserving LES (RNP-LES), the numerical results are systematically compared to experimental data. The sound field properties are especially investigated since they are typical for high Reynolds number jets with for instance broadband sideline sound spectra.¹² The final purpose is then to provide a numerical database for further investigations of noise generation mechanisms and of the effects of simulation parameters such as subgrid modellings on noise prediction.

The present paper is organized as follows. The governing equations and the numerical procedure are presented in section 2. The simulation parameters, and snapshots of vorticity and pressure are shown in section 3. The flow field and the sound field provided directly by LES are then investigated in sections 4 and 5, respectively. The flow fields obtained on the two grids are compared between each others, while all flow and acoustic results are examined with respect to the available measurements of the literature to assess the RNP-LES approach. Concluding remarks and further works are then given in section 6. Finally, a selective filtering implemented in the simulations is provided in appendix A.

2 Governing equations and numerical procedure

2.1 Filtered Navier-Stokes equations

The filtered compressible Navier-Stokes equations are solved. They are written as¹³

$$\begin{aligned} \frac{\partial \bar{\rho}}{\partial t} + \frac{\partial}{\partial x_j} (\bar{\rho} \bar{u}_j) &= 0 \\ \frac{\partial}{\partial t} (\bar{\rho} \bar{u}_i) + \frac{\partial}{\partial x_j} (\bar{\rho} \tilde{u}_i \tilde{u}_j + \bar{p} \delta_{ij} - \tilde{\tau}_{ij} - \mathcal{T}_{ij}) &= 0 \\ \frac{\partial}{\partial t} (\bar{\rho} \tilde{e}) + \frac{\partial}{\partial x_j} ((\bar{\rho} \tilde{e} + \bar{p}) \tilde{u}_j - \tilde{\tau}_{ij} \tilde{u}_j + \tilde{q}_j + \mathcal{Q}_j) - \tilde{u}_i \frac{\partial \mathcal{T}_{ij}}{\partial x_j} &= 0 \end{aligned}$$

where the flow variables ρ , u_i and p are the density, velocity and pressure, and γ is the specific

heat ratio. The overbarred quantities, *i.e.* the density, the momentum ρu_i and the pressure, are filtered explicitly using an high-order filter.¹⁰ This filtering can be regarded as the spatial LES filtering associated to the grid refinement. The other quantities are denoted by a tilde, and are calculated from the filtered variables, e.g. for the resolved velocity $\tilde{u}_i = \overline{\rho u_i} / \bar{\rho}$, and for the total energy $\bar{\rho} \tilde{e} = \bar{p} / (\gamma - 1) + \bar{\rho} \tilde{u}_k \tilde{u}_k / 2$.

The resolved viscous stress tensor $\tilde{\tau}_{ij}$ is defined by $\tilde{\tau}_{ij} = 2\mu(\tilde{S}_{ij} - \tilde{S}_{kk}\delta_{ij}/3)$ where $\tilde{S}_{ij} = (\partial\tilde{u}_i/\partial x_j + \partial\tilde{u}_j/\partial x_i)/2$ and μ is the molecular dynamic viscosity. The heat flux is given by $\tilde{q}_j = -\lambda\partial\tilde{T}/\partial x_j$ where the resolved temperature \tilde{T} is deduced from the filtered density and pressure using the equation of state $\bar{p} = \bar{\rho}r\tilde{T}$, and $\lambda = \mu c_p / \sigma$ is the thermal conductivity (σ is the Prandtl number, and c_p is the specific heat at constant pressure). The spatial filtering of the Navier-Stokes equations makes appear different terms, referred to as subgrid terms, which can not be directly calculated from the resolved variables.¹³ Among them, the two following ones are usually kept: the subgrid turbulent stress tensor $\mathcal{T}_{ij} = \overline{\rho u_i u_j} - \overline{\rho u_i} \overline{u_j}$ and the pressure-velocity subgrid term $\mathcal{Q}_j = -(\overline{p u_j} - \bar{p} \overline{u_j}) / (\gamma - 1)$.

The modelling of the subgrid stress tensor is in debate for a long, see discussions in recent reviews.¹⁴⁻¹⁶ It is well agreed that, since the energy-dissipating scales are not resolved, the addition of an artificial damping is required. This is classically done through subgrid models based on an eddy-viscosity hypothesis and built up from physical considerations, such as for the famous Smagorinsky model.¹⁷ However, since the eddy viscosity has the same functional form as the molecular viscosity, there are difficulties to define the effective Reynolds number of the simulated flow.¹⁸ An alternative to the eddy viscosity is to damp the turbulent energy by numerical methods,¹⁹ but the question about the effective Reynolds number remains as long as dissipative numerical schemes are used.

In the present simulation of a high Reynolds number jet, we set $\mathcal{T}_{ij} = 0$ and $\mathcal{Q}_j = 0$, and we use a highly-selective filtering to remove only the high waves numbers close to the grid cut-off wave number. Thus the resolved large scales are dissipated neither by an eddy-viscosity model nor by the numerical algorithm. In that sense, the present simulation can be considered as a Reynolds-Number-Preserving LES (RNP-LES). The efficiency of this kind of simulation must now be demonstrated by the comparison of the computed results with the experimental data. Further works are also required to study carefully the effects of the different formulations of subgrid models on flow and sound.²⁰

2.2 Numerical methods

The discretization of the filtered Navier-Stokes equations is taken into account by numerical schemes with properties optimized in the wave-number space ensuring accuracy up to four point par wavelength.¹⁰ As a consequence, the fluctuations discretized by four points per wavelength or more are neither distorted nor dissipated by the numerical procedure. A thirteen-point stencil finite-difference scheme and a six-stage low storage Runge-Kutta algorithm are used for the spatial derivations and the time integration, respectively. For stability, grid-to-grid oscillations are eliminated every two iteration by filtering the density, momentum and pressure using highly-

selective filters with a thirteen-point stencil in the Cartesian directions and a twenty-one-point stencil in the diagonals of the three corresponding sections (see Appendix A). Moreover, the Cartesian mesh grid is slightly non uniform with a typical stretching rate of 2%, in order to use different discretizations inside and outside the jet flow while preserving the low dispersive and low dissipative properties of the schemes.

Efficient non-reflective boundary conditions are implemented in the LES solver to minimize the magnitude of the acoustic waves reflected at the computational domain, and thus to permit the Direct Noise Computation. They combine a formulation¹¹ of sound waves in the acoustic far-field, with a sponge zone in the outflow region to dissipate flow fluctuations before they reach the boundary. The sponge zone is based on a grid stretching coming with a Laplacian filtering.¹¹ Finally, since the boundary conditions relies on equations written on the fluctuating quantities alone, adjustment terms have been added to impose the values of the mean quantities: outside the flow, mean density and mean pressure are set to the ambient density and pressure, and at the jet inflow, all the mean variables are set to the initial flow values.

3 Simulation parameters and results

3.1 Jet inflow

A circular isothermal jet at flow conditions $M = u_j/c_a = 0.9$ is investigated. This high Mach number is of interest for aeronautic applications, and is also appropriate to keep the computation at an affordable cost and to make the direct calculation of the acoustic field easier by enhancing the sound pressure levels. It corresponds also to a value found in a large amount of experimental studies of the literature, providing both aerodynamic results,²¹⁻²⁴ and acoustic results.^{12,25,26} The jet diameter is chosen as $D = 2$ cm, defining a Reynolds number $Re_D = 4 \times 10^5$ which is quite high with respect to the range of Reynolds numbers usually considered in LES ($10^3 \leq Re_D \leq 10^5$).

For high Reynolds numbers $Re_D \geq 10^5$, the jet exit boundary layers are very thin²⁷ with a momentum thickness of the order of $10^{-3}D$, and the number of points necessary for its discretization would be exorbitant. Therefore in the present simulation, the jet inflow conditions have been modeled by imposing mean flow profiles while using an random excitation to seed the turbulence. The mean inflow longitudinal velocity $u(r)$ is given by the hyperbolic-tangent profile

$$\frac{u_0(r)}{u_j} = \frac{1}{2} + \frac{1}{2} \tanh\left(\frac{r_0 - r}{2\delta_\theta}\right)$$

where u_j is the inflow centerline velocity, δ_θ the initial momentum thickness of the annular shear layer, and r_0 the jet radius. Pressure is taken as the ambient pressure, radial and azimuthal velocities are set to zero. The mean density profile is given by the Crocco-Buseman relation

$$\frac{\rho_0(r)}{\rho_j} = \left(1 + \frac{\gamma - 1}{2} M^2 \frac{u_0(r)}{u_j} \left(1 - \frac{u_0(r)}{u_j}\right)\right)^{-1}$$

for an isothermal jet. The ratio between the jet radius and the shear-layer momentum thickness r_0/δ_θ is directly connected to the number of grid points in the jet diameter, and therefore is

clearly limited in 3-D simulations. The present ratio is chosen as $r_0/\delta_\theta = 20$, which is large enough to allow the development of turbulent structures in the shear zone. The profile of the inflow longitudinal velocity thus obtained is represented in Figure 2.

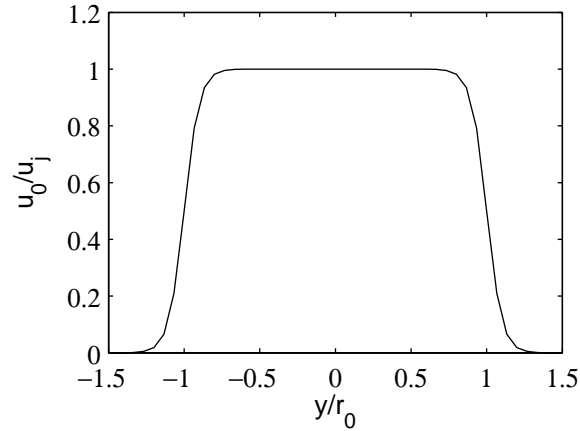


Figure 1: Transverse profile of the inflow velocity u_0/u_j at $x = 0$ and $z = 0$.

To start the turbulent flow development, the jet is forced by adding random velocity fluctuations to the mean profile, in the shear zone for $x \simeq r_0$. For the noise computation, it is important that this excitation does not radiate noise with a significant magnitude. The excitation fluctuations are therefore solenoidal⁴ and they are applied only on a few grid points at a low level. A great care is also taken to be sure that the inflow forcing is random enough not to bias the flow development. The forcing fluctuations are random both in time and in space as demonstrated by the correlation function of Figure 2.

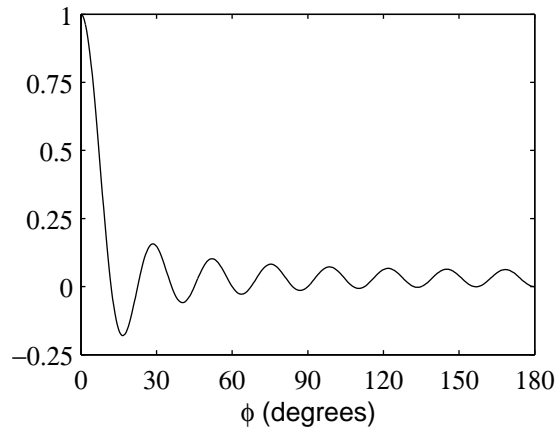


Figure 2: Azimuthal cross correlation of the forcing velocity disturbances.

3.2 Numerical specifications

The Cartesian grids used for the two simulations, referred to as LESaero and LESac in what follows, are represented in Figure 3, and contain, respectively, 16.6 and 12.5 million points. For the two grids, the discretizations in the y and z directions are the same and are symmetrical about the jet axis. The grids of LESaero and of LESac are identical in the inner zone defined by

$0 \leq x \leq 25r_0$ and $-10r_0 \leq y, z \leq 10r_0$. In this region, the transverse mesh spacing is uniform for $y \leq 3r_0$ with $\Delta y_0 = r_0/15$ and then increases at a rate of 2%, and the axial mesh spacing is constant with $\Delta x = 2\Delta y_0$. The flow field is calculated up to $x = 60r_0$ in LESaero but only up to $x = 25r_0$ in LESac. The acoustic near-field is only investigated in LESac. In the latter case, the transverse mesh spacing reaches a value of $\Delta y = 0.4r_0$ well outside the jet, which corresponds to a cut-off Strouhal number of about 2 for the sound field.

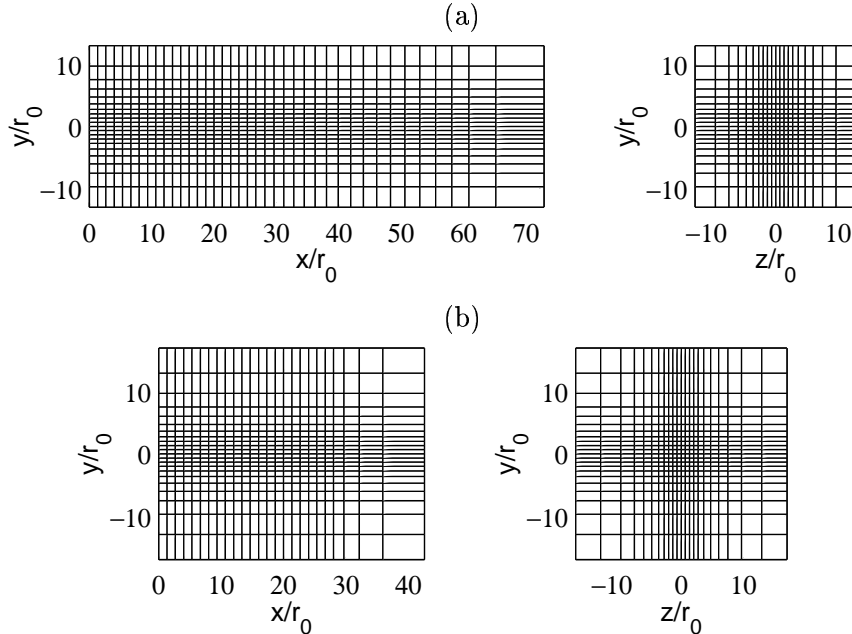


Figure 3: Visualization of the $x - y$ and $y - z$ sections of the mesh grids for: (a) LESaero, (b) LESac. Only every tenth line is shown.

More parameters of the two simulations are presented in Table 1, with particularly the time periods used for computing flow and sound quantities. It should be noted that the time step is $\Delta t = 0.85\Delta_0/c_0$ for the two simulations. The computation time, and consequently the different sampling times, are long enough to achieve statistical convergence. To illustrate this, the sound field in LESac is for example studied during a period T_{ac} which can be associated to a minimum Strouhal number of $D/T_{ac}u_j \sim St \simeq 1.2 \times 10^{-3}$.

3.3 Instantaneous vorticity and pressure

Figure 4 displays instantaneous snapshots of LES quantities provided by the two simulations. For LESaero, the axial section of the vorticity $|\omega|$ is shown in Figure 4(a). For LESac, axial and transverse sections are shown in Figure 4(b), with the vorticity $|\omega|$ in the turbulent flow region and the fluctuating pressure p' outside.

The vorticity fields show a large range of vortical scales, with the presence of a fine turbulence as expected for a high Reynolds number. The axial sections illustrate the flow development from turbulent shear layers to a turbulent jet, with a spreading of the jet which is especially visible far downstream for the LESaero simulation in Figure 4(a). The shear layers appear to interact in the vicinity of $x = 10r_0$. The length of the potential core is therefore about $10r_0$, which is

	LESaero	LESac
grid ($n_x \times n_y \times n_z$)	$395 \times 205 \times 205$	$255 \times 221 \times 221$
simulation time T	$7 \times 10^4 \Delta t$	$4 \times 10^4 \Delta t$
T	$3970r_0/c_0$	$2270r_0/c_0$
$D/Tu_j \sim St$	5.6×10^{-4}	9.9×10^{-4}
flow field for	$x \leq 60r_0$	$x \leq 25r_0$
mean flow calc. during	$6.2 \times 10^4 \Delta t$	$3.6 \times 10^4 \Delta t$
turb. int. calc. during	$4 \times 10^4 \Delta t$	$2.5 \times 10^4 \Delta t$
u' -spectra calc. during	$6 \times 10^4 \Delta t$	$3.5 \times 10^4 \Delta t$
sound field for	—	$x \leq 30r_0$
calc. during	—	$3.3 \times 10^4 \Delta t$
CPU time (Nec SX5)	200 h	90 h

Table 1: Grid and time parameters of the simulations LESaero and LESac (*calc.* is used for *calculated*, *turb. int.* for *turbulence intensities*, u' is the fluctuating axial velocity).

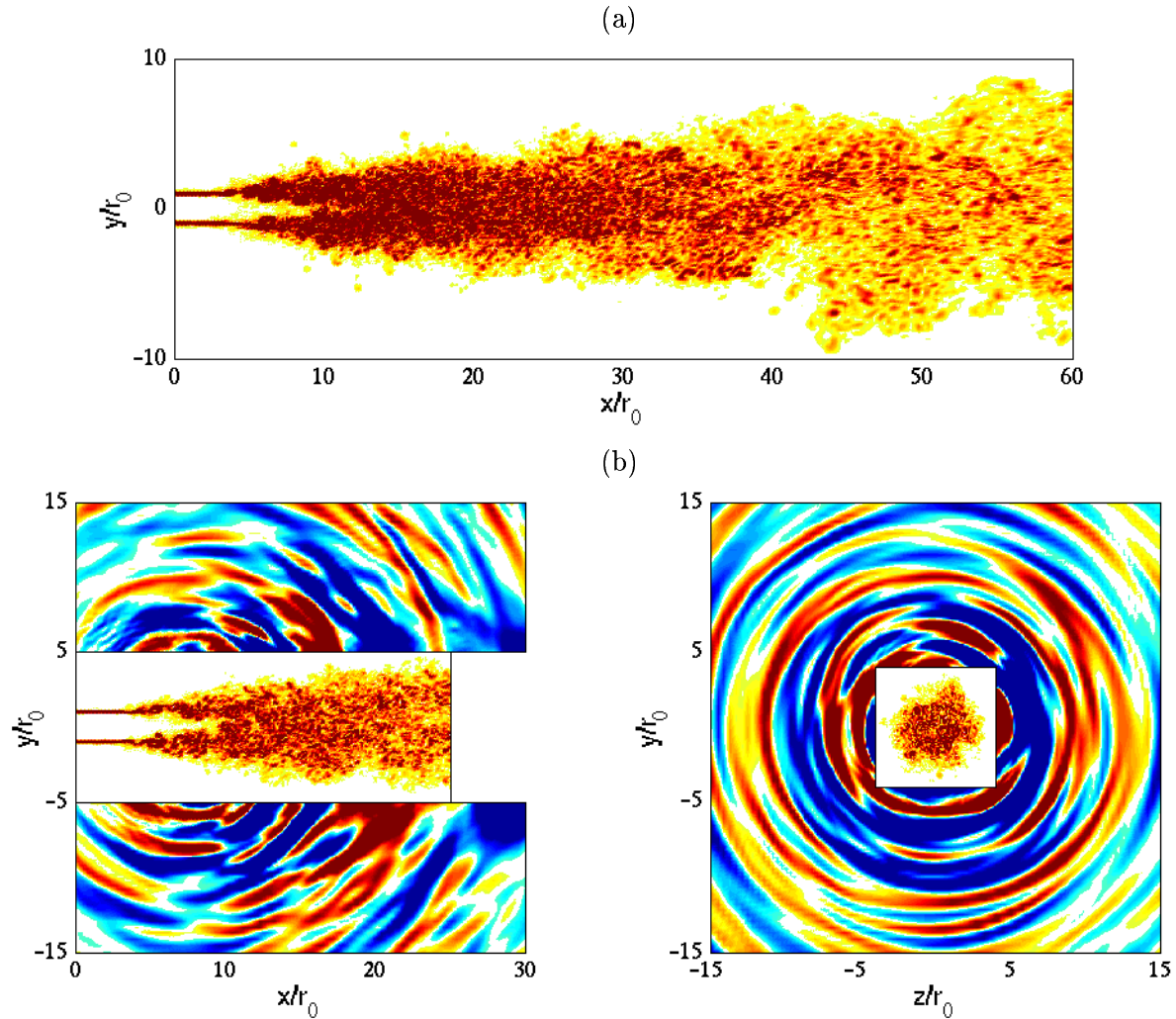


Figure 4: (a) LESaero: snapshot of the vorticity $|\omega|$. The color scale is from 0 to $4 \times 10^4 \text{ s}^{-1}$. (b) LESac: snapshots of the vorticity $|\omega|$ in the flow and of the fluctuating pressure p' outside. Left: in the $x - y$ plane at $z = 0$. Right: in the $y - z$ plane at $x = 11r_0$. The color scales are from 0 to $8 \times 10^4 \text{ s}^{-1}$ for the vorticity and from -70 to 70 Pa for the pressure.

comparable to the values measured on corresponding jets.²¹

The snapshots of the pressure fields in Figure 4(b) demonstrate that the noise generated by the jet is well taken into account by the simulation. It is properly propagated outside of the flow, and is contaminated neither by the inflow forcing, nor by possible reflections at the boundaries. The axial section shows sound waves originating from a region located in the vicinity of the end of the potential core, in agreement with experimental observations.²⁸ The acoustic radiation is also more pronounced in the downstream direction, as expected. The transverse section presents the structure of the sound waves. Waves of partially circular shape are found in the considered section at $x = 11r_0$, but they appear not to be strongly correlated azimuthally. Cross correlations will be reported in section 5 to support this observation.

4 Flow field

In this section, the flow fields computed by the LESaero and LESac simulations are investigated. Comparisons between each others, and also with experimental data are systematically made.

4.1 Mean flow

Some streamlines originating from points near the mesh boundaries are presented in Figure 5(a) for LESaero and in Figure 5(b) for LESac. They illustrate the entrainment of the surrounding fluid in the jet, and demonstrate that the boundary conditions are well appropriate for the incoming of fluid into the computational domain in both simulations. Fairly parallel to the jet near the inflow, the streamlines are more perpendicular to the flow direction as the axial distance increases and as the jet becomes turbulent. This is in good agreement with experimental observations.²⁹

Contours of the mean axial velocity are also shown in Figures 5(a) and 5(b). The solid lines associated to velocities of $0.55u_j$, $0.75u_j$ and $0.95u_j$, obtained for LESaero and for LESac, are in good agreement. This supports that the mean flow developments provided by the two simulations are the same.

To study more quantitatively the mean flow, the axial profiles of the centerline velocity u_c and of the jet half-width $\delta_{0.5}$ are represented in Figures 6(a) and 6(b). The profiles obtained from LESaero and from LESac are superposed, which demonstrates that the mean flows computed by the two simulations using computational domains of different sizes are identical, and do not depend on the location of the mesh boundaries.

As expected according to the vorticity snapshots, the velocity decay starts at the end of the potential core for about $x \simeq 10r_0$ in Figure 6(a). The decay is successfully compared with the one measured by Lau *et al.*²¹ for a similar jet. A small deceleration of the centerline velocity is also detected for about $x = 5r_0$. It is interesting to note that this behaviour within the potential core has been observed experimentally.³⁰ The evolution of the jet half-width in Figure 6(b) shows that the jet spreads slowly before the end of the potential core, but quite rapidly and

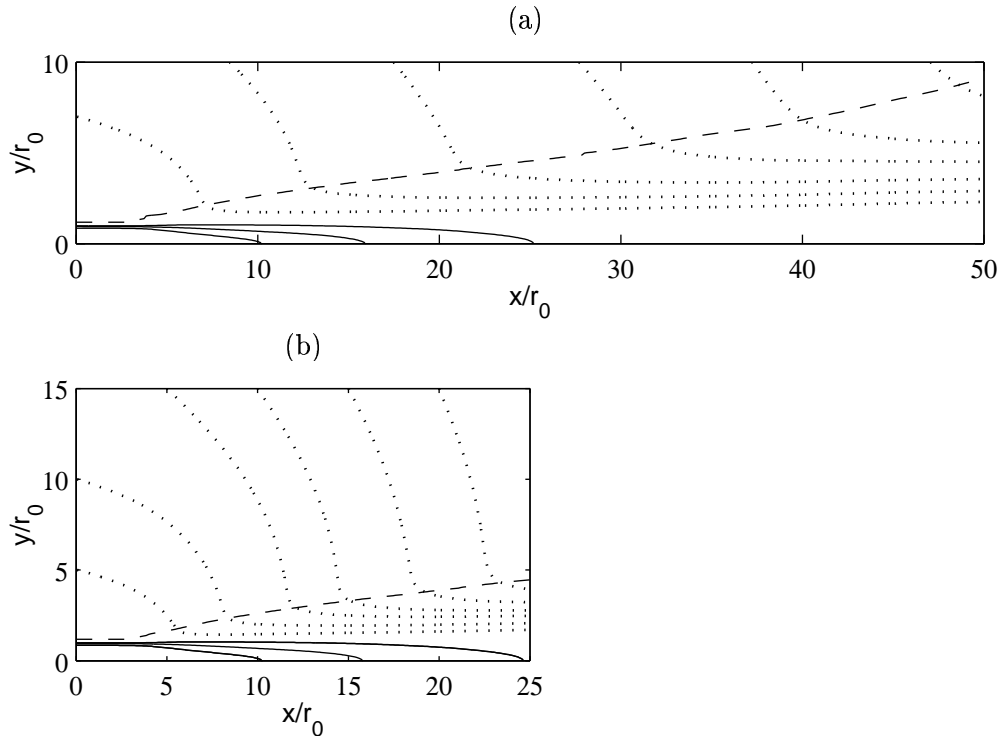


Figure 5: Visualization of the mean velocity fields for: (a) LESaero, (b) LESac. — contours associated with the mean axial velocities $0.55u_j$, $0.75u_j$ and $0.95u_j$, - - - contour associated with $0.03u_c$ (u_c is the mean centerline velocity), mean streamlines.

apparently linearly after. There is also a fair agreement with the measurements of Zaman³¹ in the region just after the end of the potential core.

In the jet literature, the mean flow is usually investigated far downstream from the nozzle, for $x > 60r_0$ at least,³² where the self-similarity of the mean profile is observed. In this zone, the velocity decay and the jet spreading are characterized by two parameters, the decay constant B and the spreading rate A , such as $u_c/u_j = B \times (2r_0/(x - x_0))$ and $\delta_{0.5} = A \times (x - x_0)$. In the present study, since the self similarity may not be reached owing to the limited size of the computational domain, the local decay constant $B = (1/2) [d(u_j/u_c)/d(x/r_0)]^{-1}$ and the local spreading rate $A = d\delta_{0.5}/dx$ are calculated and they are given in Figures 7(a) and 7(b) for $20r_0 \leq x \leq 60r_0$. The variations of B and A with the axial distance indicate clearly that the self-preserving jet zone is not reached and would require a mesh extending further downstream. However, it appears also that B and A may tend, as x increases, to values of about 6 and 0.09, respectively. These asymptotic values are in accordance with the values of B and A measured in the jet self-similarity region^{33,34} The mean flow obtained by LES is therefore in agreement with experimental data both for the transitional region after the end of the potential core and for the self-similarity region likely to be found further downstream.

4.2 Turbulence intensities

The centerline profile and the radial profile for $x = 20r_0$ of the turbulent axial velocity $\langle u'u' \rangle^{1/2}/u_j$ are plotted in Figures 8(a) and 8(b), for LESaero and LESac. Results provided

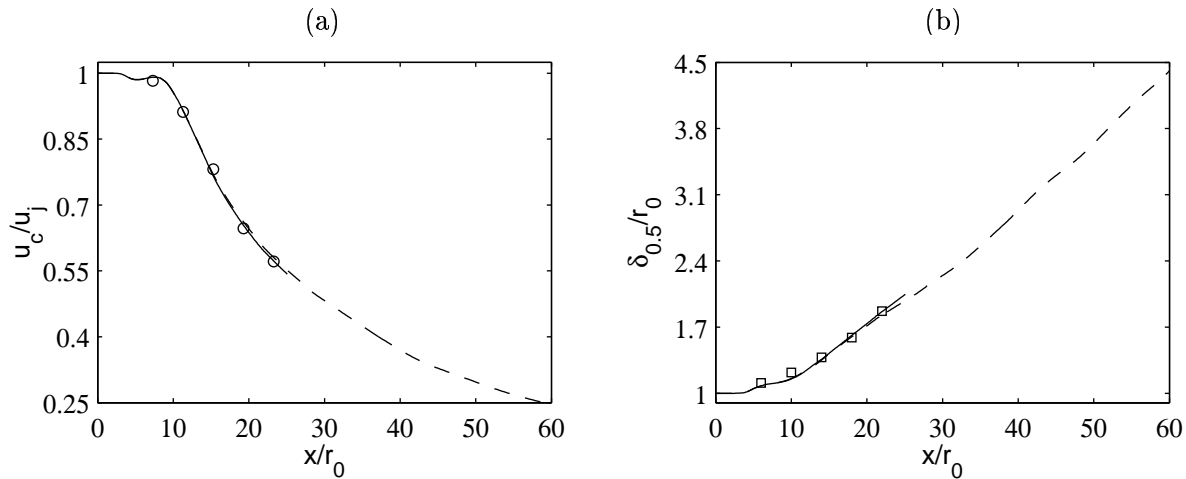


Figure 6: Axial profiles, (a), of the mean centerline velocity u_c/u_j and (b), of the jet half-width $\delta_{0.5}/r_0$ for: - - - LESaero and — LESac. Measurements: \circ Lau *et al.*²¹ ($M = 0.9$, $Re_D = 10^6$), \square Zaman³¹ ($M = 0.5$, $Re_D = 3 \times 10^5$), both shifted in the axial direction for the comparison.

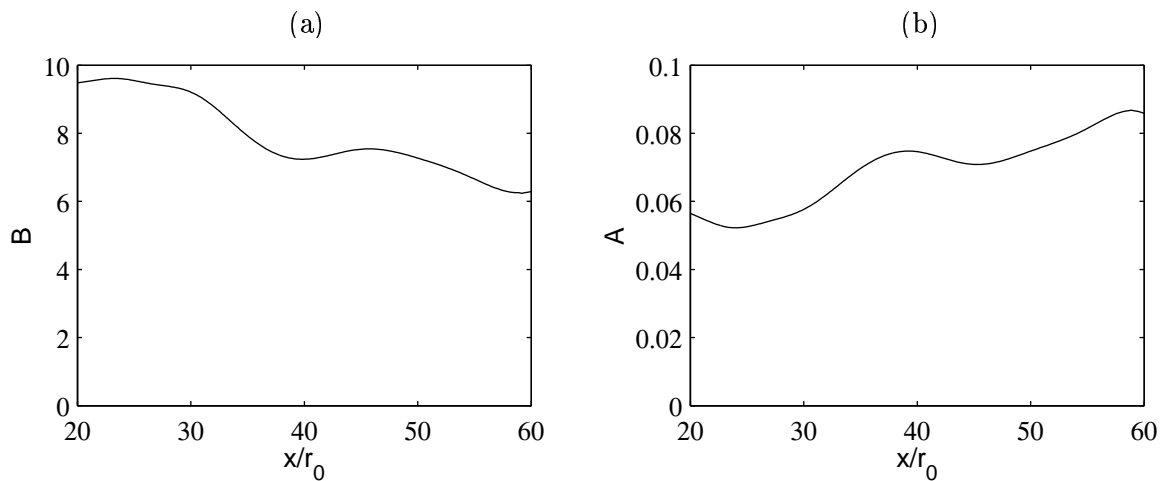


Figure 7: Axial profiles, (a), of the local centerline velocity decay constant $B = (1/2) [d(u_j/u_c)/d(x/r_0)]^{-1}$ and (b), of the local spreading rate $A = d\delta_{0.5}/dx$ for LESaero.

by the two simulations are in good accordance, and this is especially striking for the radial profiles in Figure 8(b) which are exactly superposed. As for the mean flow, the location of the boundaries of the computational domain does not affect the development of the turbulence in the jet.

The axial profile in Figure 8(a) reaches a peak for about $x = 14r_0$, slightly after the end of the potential core, in the transition region where the turbulent shear layers merge. The increase and the peak value of the turbulent velocity are compared successfully to data provided by recent Particle Image Velocimetry (PIV) measurements on Mach number $M = 0.9$, similar Reynolds number jets. These comparisons support that the jet transition is well described by the LES. This is of importance with the aim of Direct Noise Computation, since the end of the potential core is known as a region of significant noise generation.

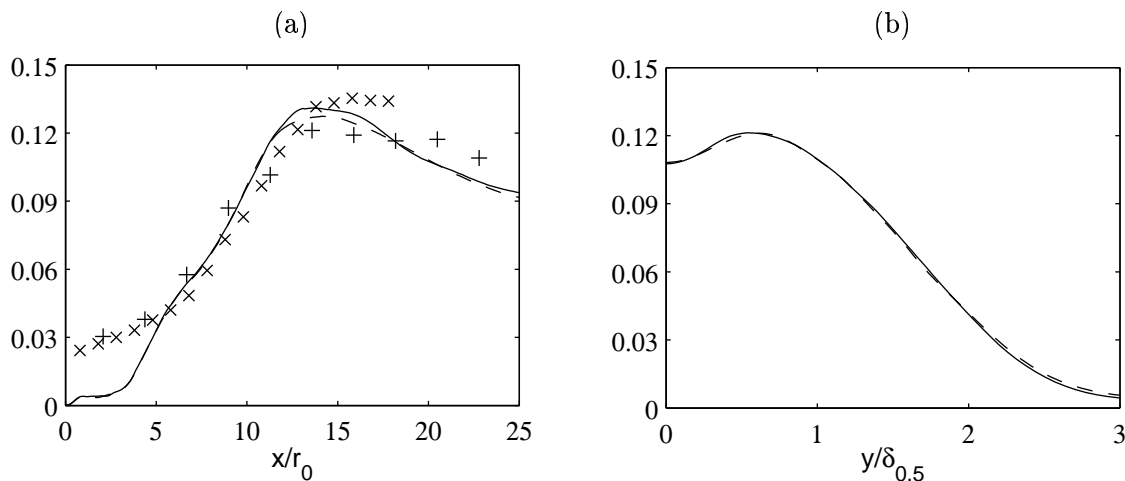


Figure 8: (a) Centerline profile and (b) radial profile for $x = 20r_0$ of the turbulent axial velocity $\langle u'u' \rangle^{1/2}/u_j$ for: - - - LESaero, ——— LESac. Measurements: \times Jordan *et al.*²³ ($M = 0.9$, $Re_D = 10^6$), $+$ Arakeri *et al.*²⁴ ($M = 0.9$, $Re_D = 5 \times 10^5$), both shifted in the axial direction for the comparison.

For the study of the turbulent region, the turbulence intensities calculated using the local centerline velocity u_c are investigated. In a high Reynolds number jet, experiments³² have shown that the turbulence intensities become self-similar only around 100 radii downstream from the nozzle, where, for example, $\langle u'u' \rangle^{1/2}/u_c \simeq 0.25$ on the jet axis.^{33,34} Therefore in the present simulation, the self-similarity plateau may not be reached. This is supported by the centerline profile of $\langle u'u' \rangle^{1/2}/u_c$ presented in Figure 9(a). The turbulence intensity increases regularly in the same way as in the experiment of Arakeri *et al.*,²⁴ and tends to a value in agreement with the measured self-similar value of 0.25. Then, the radial profiles of the turbulence intensities are represented in Figure 9(b) for $x = 50r_0$. Although their values on the jet axis are slightly lower than the ones measured in the jet self-preserving region, their relative shapes agree well with measurements.^{33,34}

4.3 Integral length scales

The integral length scales on the jet axis are now investigated. For this, the correlation

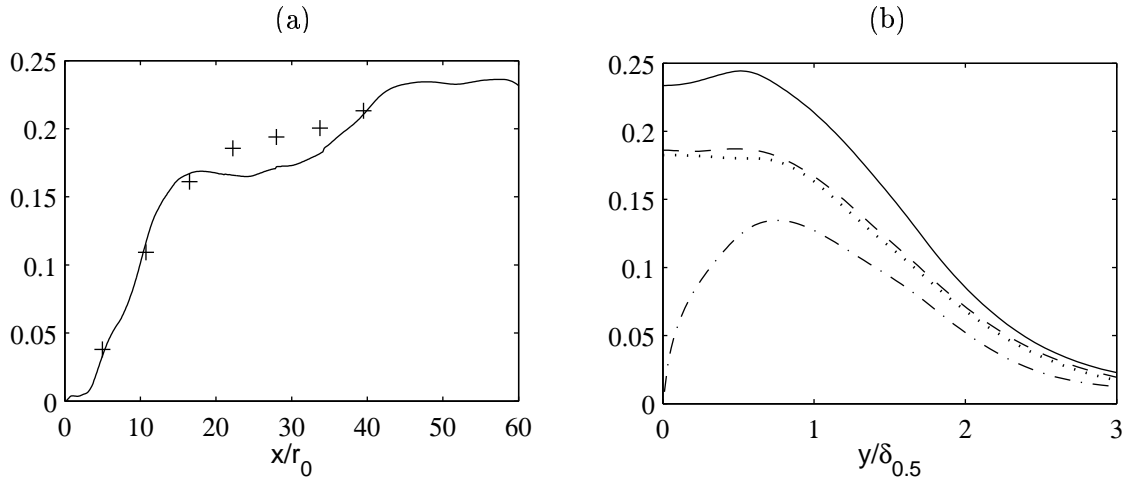


Figure 9: (a) Centerline profile and (b) radial profiles for $x = 50r_0$ of the turbulence intensities for LESaero: — $\langle u'u' \rangle^{1/2}/u_c$, - - - $\langle v'v' \rangle^{1/2}/u_c$, $\langle w'w' \rangle^{1/2}/u_c$, - · - · $\langle u'v' \rangle^{1/2}/u_c$, + measurements of Arakeri *et al.*²⁴ ($M = 0.9$, $Re_D = 5 \times 10^5$) shifted spatially for the comparison.

function of the axial fluctuating velocity $R_{11}^{(1)}(r)$ are calculated for points located at $(x, y = 0, z = 0)$ by

$$R_{11}^{(1)}(r) = \frac{\langle u'(x+r/2)u'(x-r/2) \rangle}{\langle u'^2(x+r/2) \rangle^{1/2} \langle u'^2(x-r/2) \rangle^{1/2}}$$

and the longitudinal length scale is then obtained by integration such as $L_{11}^{(1)} = \int_0^\infty R_{11}^{(1)}(r) dr$. The centerline length scales of the present simulated jet are presented in Figure 10 for $10r_0 \leq x \leq 60r_0$. First, there is no significant difference between the length scales provided by the simulations LESaero and LESac, as expected according to the independence of the flow development with the grid. Second, and this is an important key point, the length scales increase linearly as observed experimentally, with a good agreement with the law measured by Wygnanski and Fiedler.³² This validates the two-point correlations of the velocity field computed by LES, and demonstrates that the jet spreading is driven by a relevant increase of the size of the turbulent scales.

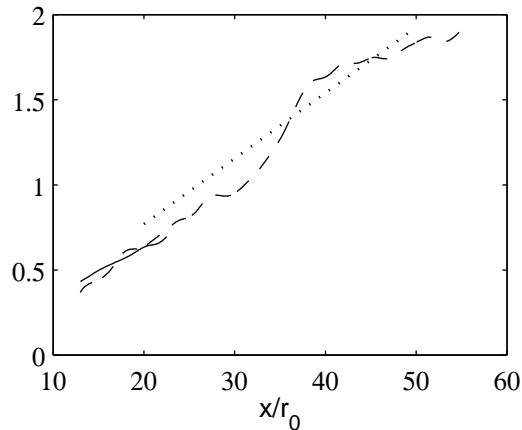


Figure 10: Axial profile of the length scale $L_{11}^{(1)}/r_0$ on the jet axis for: — LESac, - - - LESaero, line $L_{11}^{(1)} = 0.0385x$ measured by Wygnanski and Fiedler³²

4.4 Velocity spectra

The u' -velocity one-dimensional spectra $E_u^{(1)}(k_1)$ are presented in Figure 11 for $x = 20r_0$ and $x = 50r_0$ on the jet axis. They are obtained from the temporal spectrum $E_u(f)$, using the Taylor hypothesis of frozen turbulence yielding $k_1 = 2\pi f / \langle u \rangle$ and then $E_u^{(1)}(k_1) = E_f(f) \times \langle u \rangle / 2\pi$, with $\langle u \rangle$ the mean axial velocity. The computations of $E_u(f)$ for the simulations LESaero and LESac involve the final 6×10^4 and 6×10^4 iterations, as shown in Table 1. The time samplings T_{usp} are consequently such as $D/T_{usp}u_j = 6.5 \times 10^{-4}$ and 1.1×10^{-3} , and they are divided, respectively, into 341 and 199 overlapping sections. The grid cut-off wave numbers k_c are also represented in Figure 11. They are approximated by $2\pi/4\Delta x$ where Δx is the local mesh spacing in the axial direction which is larger than the spacings in the two other ones. As expected, the spectra collapse in the vicinity of k_c .

The two spectra from LESaero and LESac for $x = 20r_0$ are superposed. Their shapes are basically different from the shape of the u' -spectrum for $x = 50r_0$. The latter spectrum displays a $k_1^{-5/3}$ -like decrease just before the grid cut-off wave number, but such a behaviour is not observed for the the two former ones. Therefore an inertial zone of turbulence, where the energy is transferred from larger to smaller scales is found by the LES for $x = 50r_0$ but not for $x = 20r_0$.

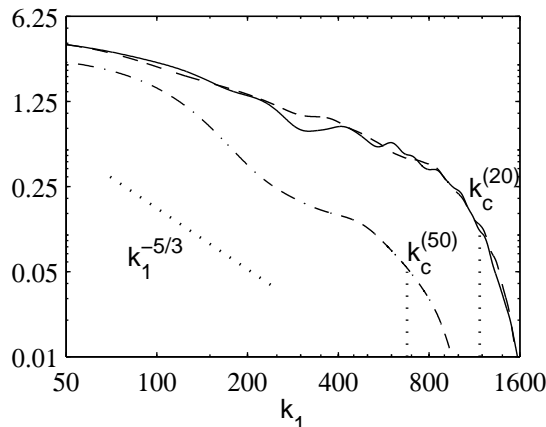


Figure 11: One-dimensional spectrum $E_u^{(1)}(k_1)$ of the fluctuating axial velocity u' , as a function of the axial wave number k_1 , and calculated on the jet axis at $x = 20r_0$, for ——— LESac and for - - - LESaero, and at $x = 50r_0$ - · - · for LESaero. $k_c^{(20)}$ and $k_c^{(50)}$ are the grid cut-off wave numbers.

To discuss this, characteristic wave numbers of the turbulence, corresponding to the axial integral scales, to the transverse Taylor scales λ_g and to the Kolmogorov scales η , are reported in Table 2 for the two points where the u' -spectra are considered. The Taylor and Kolmogorov scales are calculated using the relations of isotropic turbulence, *i.e.* $\lambda_g = (15L_{11}^{(1)}\nu/u_1')^{1/2}$ and $\eta = (L_{11}^{(1)})^{1/4}(\nu/u_1')^{3/4}$. There is a large difference between the Taylor and the Kolmogorov wave numbers, which imply that an inertial zone is likely to be found in the two cases. However, the grid cut-off wave numbers are not located identically with respect to the integral-scale wave numbers. For $x = 20r_0$, the ratio between k_c and $1/L_{11}^{(1)}$ is about 7, whereas it is about 14 for $x = 50r_0$. Thus the inertial zone for $x = 20r_0$ may not be taken into account by the grid, whereas a part of the inertial zone for $x = 50r_0$ is resolved.

	$1/L_{11}^{(1)}$	k_c	$1/\lambda_g$	$1/\eta$
$x = 20r_0$	160	1100	4800	200000
$x = 50r_0$	50	700	2300	110000

Table 2: Wave numbers associated to the axial integral length scale, to the grid cut-off, to the transverse Taylor scale and to the Kolmogorov scale, for $x = 20r_0$ and $x = 50r_0$ on the jet axis.

5 Acoustic field

The pressure field provided directly by the LESac simulation is now investigated to determine if it agrees with the one expected for a high Reynolds number, subsonic jet.

5.1 Sound pressure spectra

Sound pressure spectra are presented in Figure 12. They are calculated at four locations, defined by $x = 29r_0$ and $r = 11r_0$, by $x = 29r_0$ and $r = 15r_0$, by $x = 20r_0$ and $r = 15r_0$, and by $x = 11r_0$ and $r = 15r_0$, by averaging using 31 points equally spaced azimuthally on half a circle. In what follows, these locations are referred to by angles θ of 30° , 40° , 60° and 90° , respectively. The angles are taken from the jet axis direction, with an origin chosen around the end of the potential core where the dominant sound sources are likely to be found. As shown in Table 1, the final 3.3×10^4 iterations of the simulation are used for computing the spectra. The total time sampling T_{ac} is divided into 199 overlapping sections, and is such as $D/T_{ac}u_j = 1.2 \times 10^{-4}$ in term of Strouhal number.

The spectra of Figure 12(a) appear basically different as a function of the observation angle. The downstream spectra for $\theta = 30^\circ$ and 40° are dominated by a low-frequency component with a peak for a Strouhal number $St \simeq 0.3$. The sideline spectrum for $\theta = 90^\circ$ displays a more broadband shape with a maximum observed for $St \simeq 0.7$. Finally, the spectrum for $\theta = 60^\circ$ is halfway between the two former spectra, since its shape gathers the properties of the two other ones with two maxima for about $St \simeq 0.3$ and $St \simeq 0.7$. This modification of sound spectra as a function of the observation angle is in good agreement with the observations of the sound radiation for jets with high Reynolds numbers,¹² whereas at low Reynolds numbers, spectral shapes does not significantly differ. Therefore the effective Reynolds number of the computed jet corresponds to the Reynolds number given by the inflow conditions. This is of importance with the aim of demonstrating the feasibility of computing high Reynolds number flows by LES.

Moreover, the present LES results support the theory of jet noise proposed by Tam *et al.*³⁵ which evidenced two distinct components from a large database of spectra for both subsonic and supersonic jets: the first component radiates preferably in the downstream direction and would be associated to large scales/instability waves, and the second one dominates in the sideline and the upstream direction and would be attributed to the fine-scale turbulence. The first noise mechanism has been recently investigated by means of numerical simulations of low or moderate Reynolds number jets, and can be equally connected to the decay of instability waves² or to the periodic intrusion of vortical structures in the jet⁴ at the end of the potential core. The second

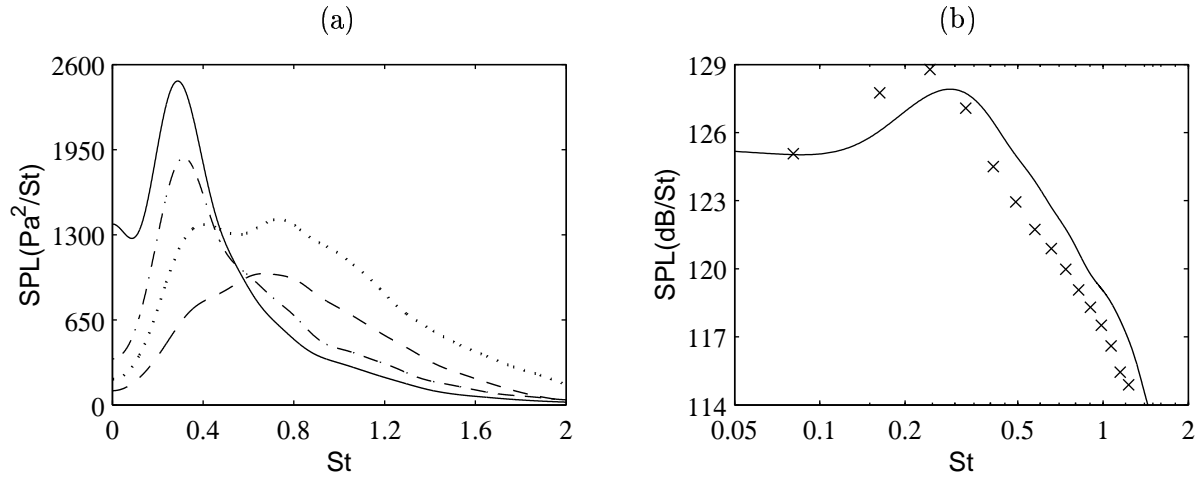


Figure 12: (a) Sound pressure spectra, in linear scales, as a function of Strouhal number $St = fD/u_j$ for: — $x = 29r_0$ and $r = 12r_0$, - - - $x = 29r_0$ and $r = 15r_0$, ····· $x = 20r_0$ and $r = 15r_0$, - · - $x = 11r_0$ and $r = 15r_0$, i.e. for angles θ from the jet axis of about 30° , 40° , 60° , 90° respectively. (b) Sound spectra, in logarithmic scales, for $\theta \simeq 30^\circ$. × measurements of Jordan *et al.*²³ ($M = 0.9$, $Re_D = 10^6$, for 30° and 60° radii from the nozzle), shifted in amplitude for the comparison of the shapes.

noise mechanism needs a sufficiently high Reynolds number to be observed, and thus can be looked into numerically only by LES.

For a more quantitative comparison of the spectra with experimental data, the downstream spectrum for $\theta \simeq 30^\circ$ is represented in Figure 12(b) with corresponding measurements of Jordan *et al.*²³ in the acoustic far-field of a similar jet, shifted in amplitude. The two computed and experimental spectral shapes are in good agreement. The peaks are obtained for close Strouhal numbers of $St \simeq 0.25$ and $St \simeq 0.30$, respectively. More strikingly, the decreases for high Strouhal numbers are quite similar, following apparently the same law. The computed spectrum seems slightly more marked for high frequencies. This little discrepancy may be due to the observation points. Measurements are made in far-field, typically in the cone of silence of the jet where high frequencies noise are lacking because of refraction effects, whereas the computed spectrum is only obtained for $x = 29r_0$ and $r = 11r_0$ where fine-scale noise may not be completely negligible. The possible presence of fine-scale noise is illustrated by the spectrum for $St \simeq 0.40$ where the high-frequency component is clearly enhanced.

The lack of acoustic spectra measured in the near acoustic field is still more acute for the study of the sideline spectrum. Far-field sideline spectra display a maximum for Strouhal $St \simeq 0.4$. The peak of the computed spectra is reached for $St \simeq 0.7$, and this is certainly due to the fact that it is obtained only at $x = 11r_0$ and $r = 15r_0$. Thus, the fine-scale noise generated in the shear-layers and at the end of the potential core is preferably observed, rather than the fine-scale noise radiated downstream. A wave-extrapolation method such as Kirchhoff method could be applied to propagate the computed sound field in far-field,³⁶ but it was not performed in the present study. The main reason is that these wave-extrapolation are not likely to bring much more informations about jet noise physics. Furthermore, to study carefully the effects on flow and sound of different parameters such as the sugrid modelings or the inflow conditions, it appears to us more relevant to focus on the near-acoustic field, even though sound measurements

for this zone would be necessary for a more complete validation.

5.2 Azimuthal cross correlations

The azimuthal cross correlations of the fluctuating pressure are now studied. They are presented in Figure 12(a) for the four observation points defined in Figure 12(a) corresponding to $\theta \simeq 30^\circ$, 40° , 60° and 90° . As for the sound spectra, the correlation functions differ greatly as a function of the observation angle. The correlation level decreases spectacularly as the angle increases, accordingly with experimental observations^{37,38} on high Reynolds subsonic jets. For $\theta \simeq 30^\circ$ and $\theta \simeq 40^\circ$, the correlation levels are very high, with for example $R_{pp} \simeq 0.4 - 0.5$ for two points symmetrically located in relation to the jet axis. For $\theta \simeq 60^\circ$ and $\theta \simeq 90^\circ$, the correlation functions decrease rapidly with the azimuth, and the sound field is only correlated over a range of about 30 degrees. There is a good correspondance between the changes in the spectra and in the azimuthal correlation. This supports the presence of two noise mechanisms in the jet: a first one associated to large scales within the jet generating downstream a highly correlated sound field, and a second one associated to turbulence and responsible for a more isotropic and decorrelated sound field.

Comparisons with experimental correlation functions are shown in Figure 12(b) for $\theta = 30^\circ$ and $\theta = 90^\circ$. For both angles, there is a good agreement with measurements of Maestrello³⁷ conducted on high subsonic jets. This validates the spatial structure of the sound field directly computed by LES.

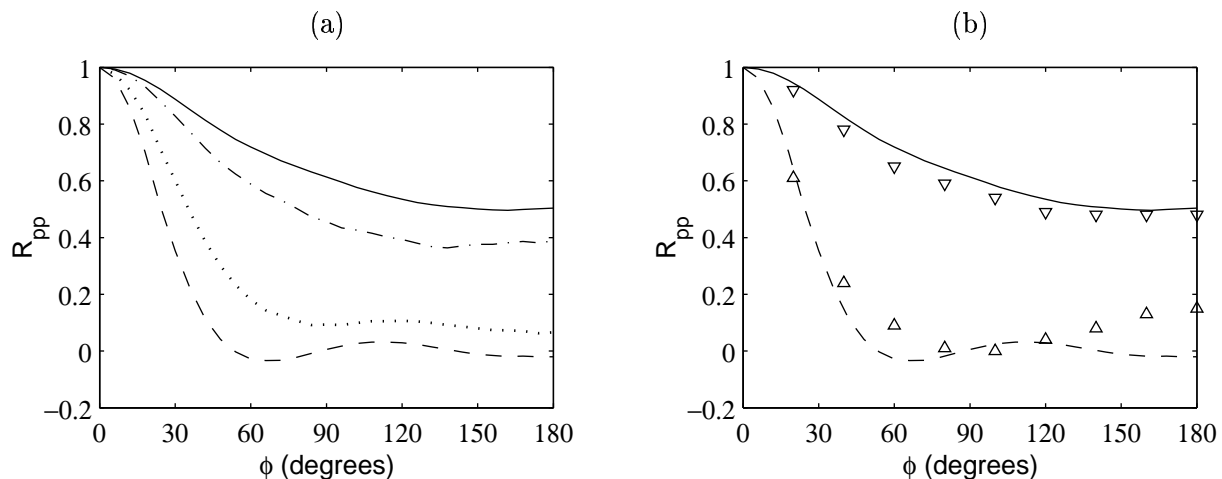


Figure 13: (a) Azimuthal cross correlations of the fluctuating pressure for: — $\theta \simeq 30^\circ$, - - - $\theta \simeq 40^\circ$, $\theta \simeq 60^\circ$, - · - $\theta \simeq 90^\circ$. (b) Comparison with measurements: ∇ Maestrello³⁷ ($M = 0.85$, $Re_D = 5.1 \times 10^5$, $\theta \simeq 30^\circ$), Δ Maestrello^{37,38} ($M = 0.7$, $Re_D = 4.3 \times 10^5$, $\theta \simeq 90^\circ$).

5.3 Sound pressure levels

Contours of the overall sound pressure levels in dB, computed by LES on the whole computational domain, are presented in Figure 14. They illustrate the strong directivity of jet noise in the downstream direction, and also show that the inflow forcing near $x = r_0$ has negligible effects on the radiated sound field. To the authors' knowledge, there are no available data of

the near-field sound pressure levels of a Mach 0.9 jet to compare with the present LES results. Moreover it might be hazardous to apply the classical $1/r$ decay law to predict the far-field sound directivity, since this method requires a large distance between the sound sources and the observation points to be reliable. This is particularly the case for the sideline sound field, generated by the fine-scale turbulence and therefore originating from an extended volume including the shear-layers as well as the developed jet.

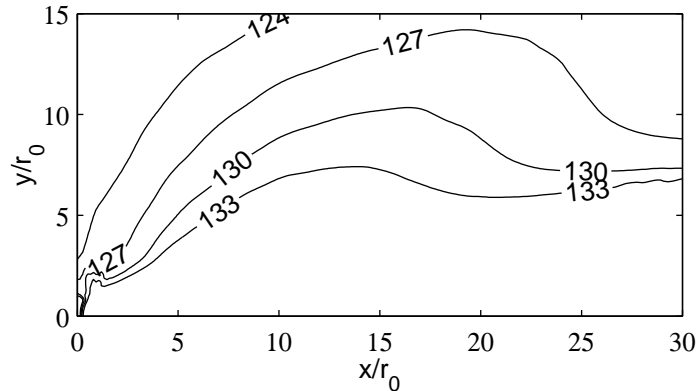


Figure 14: Contours of the overall sound pressure levels in dB.

The use of the $1/r$ decay law to predict far-field sound levels from near-field levels seems however justified for the downstream radiation which is mainly coming from the zone located at the end of the potential core.⁴ Thus, to give in the present study a simple comparison of the LES sound levels with measurements, the sound radiation at about 30° from the jet axis is considered. The sound level for the point $x = 29r_0$ and $y = 12r_0$ (125 dB) is extrapolated to a distance of 60 radii of the source region assumed to be at $x = 10r_0$ on the jet axis, using the $1/r$ decay of the acoustic waves. The computed level is 116.5 dB, which is in good agreement with well-known corresponding experimental data (Lush¹²: 115 dB, Mollo-Christensen *et al.*²⁵: 116.3 dB, Tanna²⁶: 115.5 dB).

For further investigations, dealing for instance with the effects of the subgrid-scale modellings on sound radiation, it should be interesting to study the sound levels on the near-field line $r = 15r_0$. The levels for about $x \leq 20r_0$ on this line can be mainly associated with the noise radiated by the fine-scale turbulence, which may be modified as the LES parameters varie. The profile obtained in the present LES is provided in Figure 15.

6 Conclusion

A circular isothermal jet with a Mach number $M = 0.9$ and a Reynolds number $Re_D = 4 \times 10^5$ is computed by Large Eddy Simulation (LES) on two mesh grids to investigate both the flow and the sound fields. Instead of an eddy-viscosity subgrid model, an highly selective filtering is used to ensure the dissipation of the unresolved small scales to perform a Reynolds-Number-Preserving LES (RNP-LES).

The flow fields provided by the two simulations are identical which shows the independence

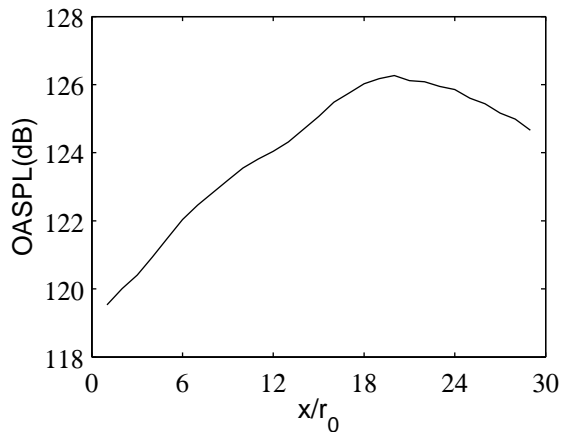


Figure 15: Overall sound pressure levels in dB for $r = 15r_0$.

of the numerical results on the location of the mesh boundaries. The mean flow and turbulence properties, as well as the sound pressure field, are in good agreement with experimental data on jets with similar conditions. The effective Reynolds number of the simulated jet appears also to correspond well to the high Reynolds number Re_D defined by the inflow conditions. This is particularly supported by the behaviour of the sound spectra and azimuthal correlations which greatly differ as a function of the observation angle. The present observations are also in accordance with the theory suggesting that there would be two components in jet noise: a first one associated to large scales, radiating preferably downstream, and a second one rather associated to the fine-scale turbulence.

The present work is a necessary preliminary step before using LES data to investigate noise generation mechanisms at high Reynolds numbers. However further works are still required to understand clearly what must be done to perform LES of jets with a full confidence. For this, the LES database provided by the present paper can be used as a reference solution, to study for instance the effects on the jet development and on its radiated sound of the different subgrid modellings proposed in the literature, or those of others parameters such as the initial shear-layer thickness.

A A 21-point stencil selective filter

To remove grid-to-grid oscillations likely to appear in the diagonals of Cartesian grid sections, a selective filter was developed. It is fourth-order only, but its coefficients d_j are optimized so that the dissipation is minimized up to $k\Delta = \pi/\sqrt{2}$, where Δ is the distance between two points located in a diagonal of a uniform mesh grid of size step Δx ($\Delta = \sqrt{2}\Delta x$). The coefficients d_j of the filter are presented in Table 3 and the corresponding damping function $D_k(k\Delta) = d_0 + \sum_{j=1}^{10} 2d_j \cos(jk\Delta)$ is displayed in Figure 16.

As for selective filters proposed previously by the authors,¹⁰ the two criteria $D_k \leq 2.5 \times 10^{-3}$ and $D_k \leq 2.5 \times 10^{-4}$ are used to provide λ_p/Δ and λ_a/Δ , *i.e.* the accuracy limits indicating the waves, respectively, properly and accurately resolved. The accuracy limits are found to be

d_0	=	0.12254360	d_6	=	0.02209702
d_1	=	-0.11724974	d_7	=	-0.01086446
d_2	=	0.10266357	d_8	=	0.00436333
d_3	=	-0.08202111	d_9	=	-0.00129033
d_4	=	0.05939469	d_{10}	=	0.00020959
d_5	=	-0.03857436			

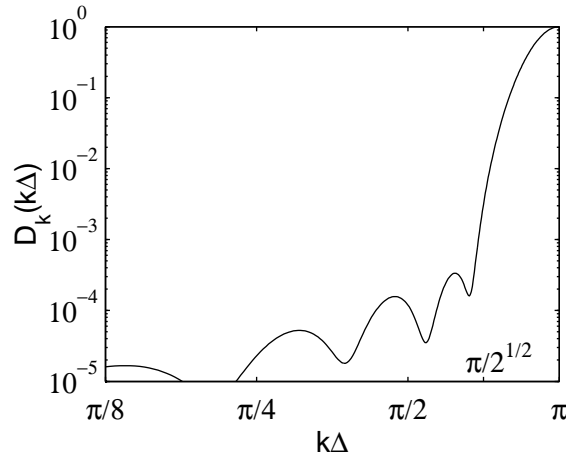
Table 3: Coefficients d_j for the selective filter on 21 points ($d_{-j}=d_j$).

Figure 16: Damping function, in logarithmic scales, of the 21-point stencil selective filter.

$\lambda_p/\Delta = 4.02/\sqrt{2}$ and $\lambda_a/\Delta = 4.76/\sqrt{2}$. These values agree well with the accuracy limit of about $\lambda/\Delta x = 4$, imposed in the Cartesian grid directions.

Acknowledgments

This work is supported by the EU Research programme JEAN (Jet Exhaust Aerodynamics and Noise) (Contract No. G4RD-CT-2000-00313). Computing time is supplied by the Institut du Développement et des Ressources en Informatique Scientifique (IDRIS - CNRS).

References

- ¹TAM, C.K.W., 1995, Computational aeroacoustics: issues and methods, *AIAA Journal*, **33**(10), 1788-1796.
- ²FREUND, J.B., 2001, Noise sources in a low-Reynolds-number turbulent jet at Mach 0.9, *J. Fluid Mech.*, **438**, 277-305.
- ³MORRIS, P.J., LONG, L.N. & SCHEIDEGGER, T.E., 1999, Parallel computations of high speed jet noise. AIAA Paper 99-1873.
- ⁴BOGEY, C., BAILLY, C. & JUVÉ, D., 2002, Noise investigation of a high subsonic, moderate Reynolds number jet using a compressible LES, to appear in *Theoret. Comput. Fluid Dynamics*. See also AIAA Paper 2000-2009
- ⁵ZHAO, W., FRANKEL, S.H. & MONGEAU, L., 2001, Large eddy simulations of sound radiation from subsonic turbulent jets, *AIAA Journal*, **39**(8), 1469-1477.

- ⁶CONSTANTINESCU, G.S. & LELE, S., 2001, Large eddy simulation of a near sonic turbulent jet and its radiated noise, AIAA Paper 2001-0376.
- ⁷UZUN, A., BLAISDELL, G.A. & LYRINTZIS, A.S., 2002, Recent progress towards a Large Eddy Simulation code for jet aeroacoustics, AIAA Paper 2002-2598.
- ⁸LUPOGLAZOFF, N., BIANCHERIN, A., VUILLOT, F. & RAHIER, G., 2002, Comprehensive 3D unsteady simulations of subsonic and supersonic hot jet flow-fields, AIAA Papers 2002-2599 and 2002-2600.
- ⁹BOGEY, C., BAILLY, C. & JUVÉ, D., 2000, Numerical simulation of the sound generated by vortex pairing in a mixing layer, *AIAA Journal*, **38**(12), 2210-2218.
- ¹⁰BOGEY, C. & BAILLY, C., 2002, A family of low dispersive and low dissipative explicit schemes for computing the aerodynamic noise, AIAA Paper 2002-2509.
- ¹¹BOGEY, C. & BAILLY, C., 2002, Three-dimensional non reflective boundary conditions for acoustic simulations: far-field formulation and validation test cases, *Acta Acustica*, **88**(4), 463-471.
- ¹²LUSH, P.A., 1971, Measurements of subsonic jet noise and comparison with theory, *J. Fluid Mech.*, **46**(3), 477-500.
- ¹³VREMAN, B., GEURTS, B. & KUERTEN, H., 1995, Subgrid-modelling in LES of compressible flow, *Applied Scientific Research*, **54**, 191-203.
- ¹⁴LESIEUR, M. AND MÉTAIS, O., 1996, New trends in large-eddy simulations of turbulence, *Annu. Rev. Fluid Mech.*, **28**, 45-82.
- ¹⁵MENEVEAU, C., AND KATZ, J., 2000, Scale-invariance and turbulence models for large-eddy simulation, *Annu. Rev. Fluid Mech.*, **32**, 1-32.
- ¹⁶DOMARADZKI, J.A. AND ADAMS, N.A., 2002, Direct modelling of subgrid scales of turbulence in large eddy simulation, *Journal of Turbulence*, **3** 024, 1-19.
- ¹⁷SMAGORINSKY, J.S., 1963, General circulation experiments with the primitive equations: I. the basic experiment, *Mon. Weath. Rev.*, **91**, 99-163.
- ¹⁸DOMARADSKI, J.A. & YEE, P.P., 2000, The subgrid-scale estimation model for high Reynolds number turbulence, *Phys. Fluids*, **12**(1), 193-196.
- ¹⁹BORIS, J.P., GRINSTEIN, F.F., ORAN, E.S. & KOLBE, R.L., 1992, New insights into large eddy simulation, *Fluid Dyn. Res.*, **10**, 199-228.
- ²⁰BOGEY, C. & BAILLY, C., 2003, LES of a high Reynolds, high subsonic jet : effects of the subgrid modellings on flow and noise, abstract submitted for the *16th AIAA Computational Fluid Dynamics Conference*, Orlando, Florida, 23-26 June 2003.
- ²¹LAU, J.C., MORRIS, P.J. & FISHER, M.J., 1979, Measurements in subsonic and supersonic free jets using a laser velocimeter, *J. Fluid Mech.*, **93**(1), 1-27.
- ²²SIMONICH, J.C., NARAYANAN, S., BARBER, T.J. & NISHIMURA, M., 2001, Aeroacoustic characterization, noise reduction, and dimensional scaling effects of high subsonic jets, *AIAA Journal*, **39**(11), 2062-2069.
- ²³JORDAN, P., GERVAIS, Y., VALIÈRE, J.-C. & FOULON, H., 2002, PIV measurements of a Mach 0.9 jet, *personnal communication*.
- ²⁴ARAKERI, V.H., KROTHAPALLI, A., SIDDAVARAM, V., ALKISLAR, M.B. & LOURENCO, L., 2002, Turbulence suppression in the noise producing region of a Mach=0.9 jet, AIAA Paper 2002-2523.
- ²⁵MOLLO-CHRISTENSEN, E., KOLPIN, M.A. & MARTUCELLI, J.R., 1964, Experiments on jet flows and jet noise far-field spectra and directivity patterns, *J. Fluid Mech.*, **18**, 285-301.

- ²⁶TANNA, H.K., 1977, An experimental study of jet noise. Part I: Turbulent mixing noise. *J. Sound Vib.*, **50**(3), 405-428.
- ²⁷ZAMAN K.B.M.Q., 1985, Far-field noise of a subsonic jet under controlled excitation, *J. Fluid Mech.*, **152**, 83-111.
- ²⁸JUVÉ, D., SUNYACH, M. & COMTE-BELLOT, G., 1980, Intermittency of the noise emission in subsonic cold jets, *J. Sound Vib.*, **71**(3), 319-332.
- ²⁹RICOU, F.P. & SPALDING, D.B., 1961, Measurements of entrainment by axisymmetrical turbulent jets, *J. Fluid Mech.*, **11**, 21-32.
- ³⁰ISLAM, M.T. & ALI, M.A.T., 1997, Mean velocity and static pressure distributions of a circular jet, *AIAA Journal*, **35**(1), 196-197.
- ³¹ZAMAN, K.B.M.Q., 1986, Flow field and near and far sound field of a subsonic jet, *J. Sound Vib.*, **106**(1), 1-16.
- ³²WYGNANSKI, I. & FIEDLER, H., 1969, Some measurements in the self-preserving jet, *J. Fluid Mech.*, **38**(3), 577-612.
- ³³PANCHAPAKESAN, N.R. & LUMLEY, J.L., 1993, Turbulence measurements in axisymmetric jets of air and helium. Part I. Air jet. *J. Fluid Mech.*, **246**, 197-223.
- ³⁴HUSSEIN, H.J., CAPP, S.P. & GEORGE, W.K., 1994, Velocity measurements in a high-Reynolds-number, momentum-conserving, axisymmetric, turbulent jet, *J. Fluid Mech.*, **258**, 31-75.
- ³⁵TAM, C.K.W., GOLEBIOWSKI, M. & SEINER, J.M., 1996, On the two components of turbulent mixing noise from supersonic jets, AIAA Paper 96-1716.
- ³⁶GLOERFELT, X., BAILLY, C. & JUVÉ, D., 2002, Noise radiated by a subsonic cavity flow and application of integral methods, to appear in *J. Sound Vib.*, see also AIAA Paper 2001-2226.
- ³⁷MAESTRELLO, L., 1976, Two points correlations of sound pressure in the far field of a jet: Experiment, NASA-TMX-72835.
- ³⁸JUVÉ, D. & SUNYACH, M., 1978, Structure azimutale du champ acoustique lointain d'un jet subsonique, *C. R. Acad. Sc., Paris*, T. 287 N.8, série B, 187-190.